The Astrophysical Journal, 777:96 (9pp), 2013 November 10 doi:10.1088/0004-637X/777/2/96

TOWARD A REMOVAL OF TEMPERATURE DEPENDENCIES FROM ABUNDANCE DETERMINATIONS: NGC 628*

Kevin V. Croxall[1,2], J. D. Smith[2], B. R. Brandl[3], B. A. Groves[4], R. C. Kennicutt[5], K. Kreckel[4], B. D. Johnson[6], E. Pellegrini[2], K. M. Sandstrom[4,14], F. Walter[4], L. Armus[7], P. Beirão[8], D. Calzetti[9], D. A. Dale[10], M. Galametz[5], J. L. Hinz[11], L. K. Hunt[12], J. Koda[13], and E. Schinnerer[4]

[1] Department of Astronomy, The Ohio State University, 4051 McPherson Laboratory, 140 West 18th Avenue, Columbus, OH 43210, USA; croxall@astronomy.ohio-state.edu
[2] Department of Physics and Astronomy, University of Toledo, 2801 West Bancroft Street, Toledo, OH 43606, USA
[3] Leiden Observatory, Leiden University, P.O. Box 9513, 2300-RA Leiden, The Netherlands
[4] Max-Planck-Institut fur Astronomie, Königstuhl 17, D-69117 Heidelberg, Germany
[5] Institute of Astronomy, University of Cambridge, Madingley Road, Cambridge CB3 0HA, UK
[6] Institut d'Astrophysique de Paris, UMR7095 CNRS, Université Pierre & Marie Curie, 98 bis Boulevard Arago, F-75014 Paris, France
[7] Spitzer Science Center, California Institute of Technology, MC 314-6, Pasadena, CA 91125, USA
[8] Observatoire de Paris, 61 avenue de l'Observatoire, F-75014 Paris, France
[9] Department of Astronomy, University of Massachusetts, Amherst, MA 01003, USA
[10] Department of Physics and Astronomy, University of Wyoming, Laramie, WY 82071, USA
[11] MMT Observatory, University of Arizona, 933 North Cherry Avenue, Tucson, AZ 85721, USA
[12] INAF-Osservatorio Astrofisico di Arcetri, Largo E. Fermi 5, I-50125 Firenze, Italy
[13] Department of Physics and Astronomy, SUNY Stony Brook, Stony Brook, NY 11794-3800, USA
Received 2013 August 1; accepted 2013 September 2; published 2013 October 18

ABSTRACT

The metal content of a galaxy, a key property for distinguishing between viable galaxy evolutionary scenarios, strongly influences many of the physical processes in the interstellar medium. An absolute and robust determination of extragalactic metallicities is essential in constraining models of chemical enrichment and chemical evolution. Current gas-phase abundance determinations, however, from optical fine-structure lines are uncertain to 0.8 dex as conversion of these optical line fluxes to abundances is strongly dependent on the electron temperature of the ionized gas. In contrast, the far-infrared (far-IR) emission lines can be used to derive an O^{++} abundance that is relatively insensitive to temperature, while the ratio of the optical to far-IR lines provides a consistent temperature to be used in the derivation of an O^{+} abundance. We present observations of the [O III] 88 μm fine-structure line in NGC 628 that were obtained as part of the Key Insights on Nearby Galaxies: a Far Infared Survey with *Herschel* program. These data are combined with optical integrated field unit data to derive oxygen abundances for seven H II regions. We find the abundance of these regions to all lie between the high and low values of strong-line calibrations and to be in agreement with estimates that assume temperature fluctuations are present in the H II regions.

Key words: galaxies: abundances – galaxies: individual (NGC 628) – galaxies: ISM – H II regions – infrared: ISM – ISM: abundances

Online-only material: color figures, extended figure

1. INTRODUCTION

Many aspects of the universe are governed by the abundance of elements heavier than He. Metals provide effective means to alter the opacities and can dominate heating and cooling, and thus determine the fundamental structure of both the interstellar medium (ISM) and stars. Extragalactic abundances can therefore be used to distinguish between viable galaxy evolutionary scenarios.

Despite this strong dependence on abundance, the calibration of nebular abundances from nebular emission lines remains uncertain at the level of ~0.8 dex (Kewley & Ellison 2008). Elemental abundances of extragalactic H II regions are primarily determined from strong collisionally excited optical emission lines. These determinations require knowledge about the electron density (n_e), the electron temperature (T_e), and the fraction of atoms in each ionic state. Detection of the temperature sensitive [O III] λ4363 line, in addition to the strong λ5007 line, enables a *direct* (Dinerstein 1990) determination of the electron temperature (Osterbrock & Ferland 2006). The [O III] λ4363 line, however, is inherently weak, making it difficult to detect. Detection is further complicated by the fact that its strength decreases as metallicity increases, since the presence of metals causes the temperature of an H II region to decrease. This makes [O III] λ4363 virtually undetectable in cooler, metal rich H II regions that are typical in spiral galaxies (e.g., see Stasińska 2005). As a result, well-constrained direct calibrations of the abundance scale are limited to metal poor H II regions.

In the absence of a direct measure of the temperature from the oxygen lines, abundances must be determined from *strong-line* techniques (e.g., Dopita et al. 2000) which rely on either empirical calibrations (i.e., Pilyugin & Thuan 2005) or photoionization models (i.e., Kobulnicky & Kewley 2004). These calibrations bring with them their own uncertainties and assumptions, which can arise from atomic data (e.g., ionic cross sections, collision strengths, and recombination coefficients) and the physical description of the model (e.g., gas distribution, chemical composition, and dimensionality). For example, Stasińska & Szczerba (2001) show that the specific dust model adopted in a photo-ionization code can alter the

* *Herschel* is an ESA space observatory with science instruments provided by European-led Principal Investigator consortia and with important participation from NASA.
[14] Marie Curie Fellow.

temperature structure of the nebula; this results in differences in the inferred temperature between 30% and 60%. Even the manner in which observations are compared with the models can affect how line ratios are interpreted. For example, Morisset & Georgiev (2009) demonstrate the importance of aperture matching in reproducing the observations of nebular emission lines. These uncertainties result in abundance scales that can differ up to 0.8 dex for a given strong-line observation (Kewley & Ellison 2008). Though the absolute scale of these strong-line calibrations may disagree, they can provide more reliable relative abundances. However, each calibration suffers from its own bias effects, making it difficult to compare published results from different studies or to establish an absolute scale.

Even in a case where the temperature sensitive line is detected, there are systematic issues related to the temperature structure of the H II region. H II regions are not simple spherical clouds uniformly filled with gas at a single temperature. Peimbert (1967) demonstrated that fluctuations in temperature within an H II region can lead to the deduction of an incorrect temperature from observations of temperature sensitive lines. This would suggest that abundances determined via the *direct* method underestimate the abundance of the ionized gas (Peimbert 1967). Abundances in extragalactic H II regions rely on observations of strong collisionally excited lines. In nearby bright H II regions, optical recombination lines are also detected. These different sets of lines, optical recombination and collisionally excited, yield significantly different temperatures for the same cloud (e.g., Esteban et al. 2009; García-Rojas & Esteban 2007). Different elements also indicate different temperatures for a given ionization zone. Nicholls et al. (2012) somewhat controversially suggest that these disagreements may be resolved by relaxing the assumption that electrons are in a Maxwellian energy distribution.

In addition to the optical forbidden lines, two strong [O III] fine-structure transitions exist in the far-infrared (far-IR), at 52 μm and 88 μm. As the metal content of an H II region increases and the temperature decreases, contributions to cooling from far-IR fine-structure lines become more important to consider (Stasińska 2002). Around an oxygen abundance of half of the solar value[15] ($12+\log(\mathrm{O/H}) \sim 8.4$), [O III] cooling becomes dominated by emission in the far-IR. Due to low excitation temperatures, if O^{++} exists in a nebula, then the far-IR lines will be emitted. Moreover, since these lines are less sensitive to the temperature of the nebula, they will be largely insensitive to temperature fluctuations, which, within and across an H II region, may lead to the inaccurate abundance determinations (e.g., Peimbert 1967). Thus, observation of these far-IR lines may enable a calibration of the metallicity scale that is largely independent of the temperature uncertainties that plague current calibration schemes.

Though inaccessible from the ground, both [O III] 88 and 52 μm lines were previously observed by the *Infrared Space Observatory* (*ISO*; Kessler et al. 1996). Brauher et al. (2008) show that, in many nearby galaxies, the emission from the [O III] 88 μm line is between 0.03% and 2% of the total far-IR dust continuum. Garnett et al. (2004) used *ISO* observations of the 88 μm and narrow band imaging of [O III] 5007 Å to derive T[O III] in M51. However, they were unable to derive an absolute oxygen abundance because (1) they lacked a direct measure of H^+, (2) they did not observe [O II], and (3) multiple H II regions were contained within the large, $\sim 80''$, *ISO* beam. Studies of the galactic ISM were able to focus on single H II regions which had measurements of H^+ from the radio continuum. Still, the absence of infrared emission lines of O^+ resulted in a reliance on ionization correction factors (Simpson et al. 2004). Given that the fractional abundance of O^{++} was less than 0.5, these abundances are uncertain. Other authors simply reported their derived abundance of O^{++} as a lower limit on the total oxygen abundance (Martín-Hernández et al. 2002). The determination of oxygen abundances from *ISO* is further complicated by the need to deduce the relative number of oxygen to hydrogen atoms within the observed aperture. Because of the large beam, this becomes difficult, since contributions from diffuse H II can contaminate large sections of imaging data that would be required to deduce the amount of H^+ in the *ISO* beam associated with the H II regions.

ISO's spatial resolution does not allow (1) extragalactic H II regions could to be isolated, (2) abundance gradients within even nearby galaxies to be studied, nor (3) far-IR observations to be matched with optical data. Consequently, no other ionization states of oxygen could be folded in to yield a total oxygen abundance from *ISO* data.

With the photodetector array camera and spectrometer (PACS) on board the *Herschel Space Observatory*, we are, for the first time, able to target the far-IR [O III] lines in nearby galaxies, among other neutral and ionized fine-structure lines, on sub-kiloparsec scales. The KINGFISH project (Key Insights on Nearby Galaxies: a Far-Infrared Survey with *Herschel*; Kennicutt et al. 2011) is an open-time *Herschel* program investigating critical dust and gas diagnostics within nearby galaxies that span a range of physical parameters (Kennicutt et al. 2011). We are able to further constrain the physical properties of the H II regions by combining the far-IR observations of the KINGFISH program with matched mid-IR observations available from the Spitzer infrared nearby galaxies survey (SINGS; Kennicutt et al. 2003). The development of optical integrated field units (IFUs) enables us to obtain optical spectral maps. With these maps, we can extract spectra from matched apertures rather than attempting to scale long slit spectra to the far-IR observations. The spectral coverage and spatial resolution of these combined observations allow us to use the temperature insensitive far-IR [O III], fine-structure lines to investigate abundance patterns in nearby galaxies.

In this paper, we present a pilot investigation of H II regions in NGC 628 by combining data from optical IFU spectroscopy with spectroscopic observations from the KINGFISH and SINGS programs. NGC 628 was selected for this as investigation due to the existence of publicly available Postdam Multi-Aperture Spectrometer (PMAS) fiber package (PPAK) data, which was obtained as part of the PPAK Integral Field Spectroscopy Nearby Galaxies Survey (PINGS; Rosales-Ortega et al. 2010). In Section 2, we present the observations and discuss the data processing. The various temperature and density dependencies are discussed and abundances are derived in Section 3. Finally, we summarize the results of this study in Section 4.

2. OBSERVATIONS

2.1. Far-IR PACS Maps

Using PACS on board *Herschel*, we carried out far-IR spectral observations of the [O III] 88 μm line within NGC 628 as part of the KINGFISH Open Time Key Program (Kennicutt et al. 2011). We report a detailed summary of observations in Table 1. The

[15] We have assumed the solar oxygen abundance of Asplund et al. (2009), $12+\log(\mathrm{O/H}) = 8.69 \pm 0.05$.

Table 1
PACS Spectroscopic Observations of NGC 628

Obs. ID	R.A. (J2000)	Decl. (J2000)	Raster Pattern	Raster Step (″)	Duration (s)	Repe-titions	$t_{[O\,III]}$ (s)
1342223786	1 36 35.50	+15 50 11.0	2 × 2	4.5 × 4.5	3,202	2	1,200
1342223784	1 36 38.80	+15 44 25.0	2 × 2	4.5 × 4.5	3,228	1	600
1342223781	1 36 37.50	+15 45 12.0	2 × 2	4.5 × 4.5	3,230	1	600
1342223779	1 36 45.10	+15 47 51.0	2 × 2	4.5 × 4.5	3,215	1	600
1342223777	1 36 41.80	+15 47 00.0	13 × 2	23.5 × 4.5	16,692	2	7,800

Notes. Summary of PACS spectral observations of [O III] NGC 628. Units of right ascension are hours, minutes, and seconds, and units of declination are degrees, arcminutes, and arcseconds. Multiple lines were found in each observation. The duration is the full time of the observation, and $t_{[O\,III]}$ is the portion of the observation devoted to the [O III] line at 88 μm.

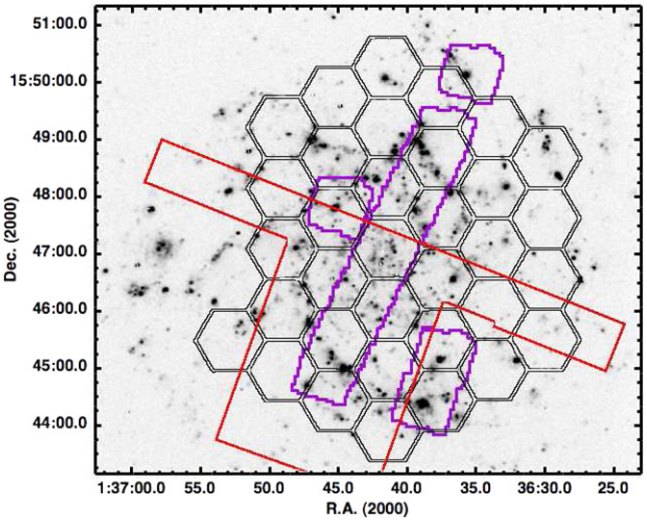

Figure 1. Footprints of PINGS, KINGFISH, and IRS observations of NGC 628 shown in black, purple, and red, respectively, overlaid on the Hα image from SINGS. The hexagonal pattern seen in the PINGS footprint is the PMAS IFU shape, each tile represents an individual pointing. IRS observations are a combination of a long strip from SINGS and a wider strip covering the south. The PACS data from KINGFISH are assembled from pointings of the ∼47″ field-of-view that are observed as a strip and individual extranuclear regions. Offsets between PINGS observations of NGC 628 are corrected by aligning the peak Hα emission in individual hexagonal tiles of the PINGS map with the SINGS Hα map.

(A color version of this figure is available in the online journal.)

IFU on board PACS has a roughly 47″ × 47″ field of view, which comprises 25 9.″4 × 9.″4 spatial elements (Poglitsch et al. 2010). In Figure 1, we show footprints of the spectral observations of NGC 628. Far-IR observations were designed to be aligned with existing observations with the *Spitzer* Infrared Spectrograph (IRS; Houck et al. 2004).

All PACS spectral observations were obtained in the un-chopped mapping mode and reduced using the Herschel Interactive Processing Environment (HIPE) version 8.0 (Ott 2010). Reductions applied the standard spectral response functions, flat field corrections, and flagged instrument artifacts and bad pixels (see Poglitsch et al. 2010; Kennicutt et al. 2011). The dark current, determined from each individual observation, was subtracted during processing because it was not removed via chopping. In-flight flux calibrations were applied to the data. These calibrations resulted in absolute flux uncertainties on the order of 15% with relative flux uncertainties between each *Herschel* pointing on the order of ∼10%.

Initial processing assumed that *Herschel's* baseline was stable for the duration of the observation. However, baseline drifts and long term instrumental transients occur and cause the non-astrophysical continuum, which is dominated by emission from *Herschel* itself, level to drift. These transients were strongly correlated with motions of the grating and of *Herschel*. Indeed, modeling of the spectral energy distributions of KINGFISH galaxies (Dale et al. 2012) has indicated that less than 2% of the spectral continuum was astrophysical. Thus, we assume that continuum emission from dust is undetected, and we use observations of the continuum region next to the [O III] 88 μm line to correct for transients. This significantly improves our ability to detect line emission. We subtract averages of the clean off-observations obtained from observations to correct for the thermal background contributed by *Herschel*. Subsequently, all spectra within a given spatial element are combined. We create final spectral cubes with 2.″85 spatial pixels by projecting dithered raster positions of each spectral line together. The final [O III] map is shown overlaid on the SINGS Hα image in Figure 2. Extracted PACS spectra are shown in Figure 3 for each of the regions labeled in Figure 2.

2.2. PPAK Data

NGC 628 was observed with the PMAS (Roth et al. 2005) using the PPAK IFU as part of the PINGS Survey (Rosales-Ortega et al. 2010). By tiling observations of NGC 628, PINGS has produced emission line maps for several strong optical lines (Sánchez et al. 2011), see Figure 1. Initial registration of emission line maps of NGC 628 was performed by matching stellar sources to optical images taken as part of the SINGS survey (Sánchez et al. 2011). However, this registration did not account for offsets that existed between the different pointings (F. F. Rosales-Ortega 2012, private communication). To account for these offsets, we re-registered the PINGS emission line maps of NGC 628, on a tile-by-tile basis, with Hα imaging from SINGS (Muñoz-Mateos et al. 2009).

Because we are working with both optical and far-IR observations, it is essential that we convolve the data to a matched resolution. The individual fibers of PPAK are 2.″7 in diameter, and thus require convolution to ensure a valid comparison of fluxes from the disparate data sets. Observations of calibration stars show that the point spread function (PSF) that PPAK produces is well matched by a top-hat profile. A convolution kernel was made following the work of Aniano et al. (2011) to match a 2.″7 diameter top hat to the PSF of PACS at 88 μm (∼9″). The convolved PINGS spectral mapping of Hα is shown in Figure 2.

PINGS observations of NGC 628 were only dithered in the central pointing, leaving the remaining tiles (including those containing our regions) with incomplete spatial coverage. To correct for this incomplete spatial coverage (i.e., aperture bias),

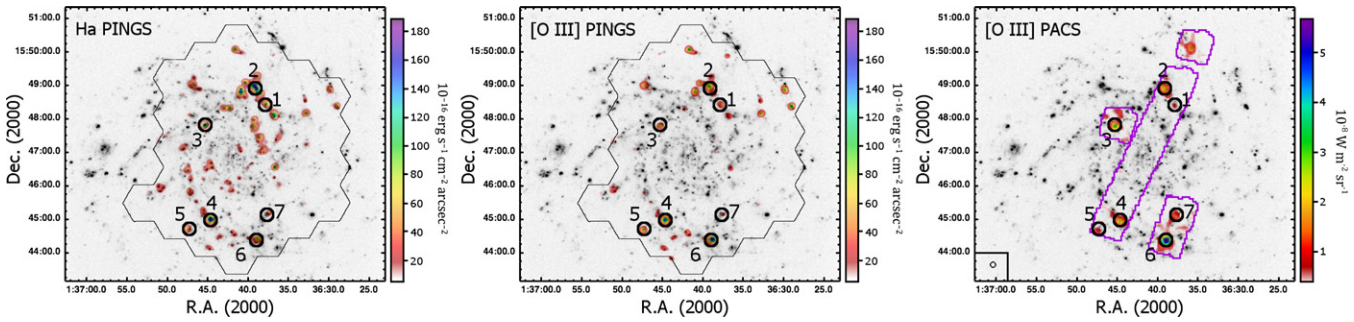

Figure 2. Spectral maps of PINGS Hα (left) and [O III] 5007 Å (center) convolved to match the *Herschel* beam at 88 μm and KINGFISH [O III] 88 μm emission (right) in NGC 628, all overlaid on the continuum subtracted SINGS Hα image. We number the regions that were extracted for abundance determinations. We require that regions were robustly detected in both PINGS and KINGFISH spectral datasets for consideration in this study. The extraction size was chosen to be larger than the beam size, shown in the lower corner of the [O III] plot, to ensure extended emission was not associated with each H II region, which was missed by the extraction. Footprints of the mapped area are denoted by the thin black lines.

(A color version of this figure is available in the online journal.)

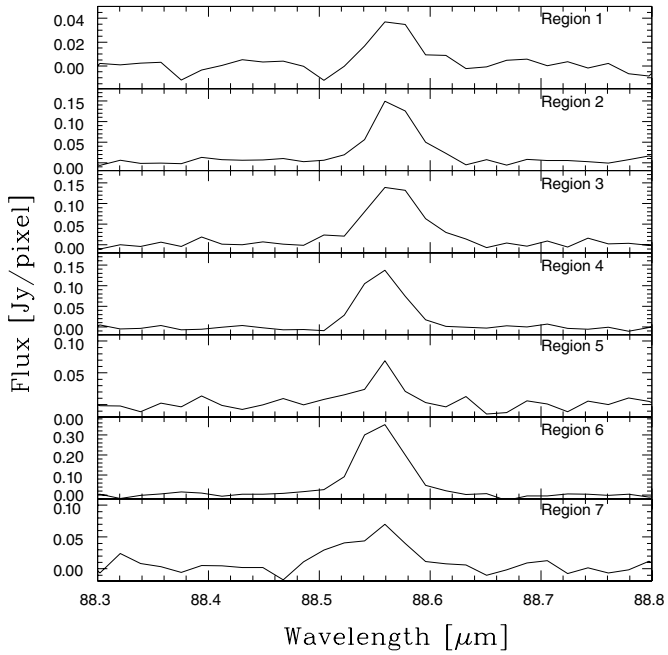

Figure 3. Extracted PACS spectra of the [O III] 88 μm line for each of the seven regions presented in this study.

we use SINGS narrow-band Hα images (Muñoz-Mateos et al. 2009). From these narrow-band images, we determine the Hα flux of our regions, corrected for N II contamination, and use the ratio of this flux to the spectroscopic Hα flux to scale all the line fluxes measured from the PINGS spectroscopy. These scale factors ranged between 5 and 30 with a typical value of $\sim$10. Though other species of ionized gas may have distributions that are different from H^+, these differences are likely to be small relative to the size of the apertures used. The correction for [N II] contamination of the Hα images was determined using the PINGS spectroscopy, from which we derived [N II]/Hα between 0.24 and 0.50, with an average value of 0.37 for the regions investigated in this paper. This is similar to the average value of 0.345 $\pm$ 0.046, derived by Kennicutt et al. (2009), and the value of 0.408 $\pm$ 0.168, derived from the driftscan observations of Moustakas et al. (2010).

We determine the dust reddening estimates by comparing the observed ratios of Balmer emission line fluxes to intrinsic ratios. Ratios of intrinsic Balmer line strength were interpolated from the tables of Hummer & Storey (1987) for Case B recombination (Hα/Hβ = 2.86) using the extinction curve of O'Donnell (1994). We assume that the flux from the [O III] 88 μm line is un-extinguished. Reddening corrected line fluxes relative to Hβ are reported in Table 2 for the 7 H II regions analyzed in this paper, as indicated in Figure 2.

2.3. IRS Data

NGC 628 was also observed by the SINGS program (Kennicutt et al. 2003) with *Spitzer*-IRS (Houck et al. 2004). The observed wavelength range includes the [Ne II] and [Ne III] lines at 12.8 and 15.6 μm, respectively, and the [S III] lines at 18.7 and 33.5 μm. These lines can be used to constrain the metallicity, ionization state, and density of an H II region. Both the nuclear and extra-nuclear regions were targeted by the short–low (SL) module. In addition to SL observations, the long–low (LL) module targeted strips across each target galaxy (see Figure 1). Additional SL and LL data were obtained for NGC 628 by *Spitzer* Program JDSMITH_PBM/20518. For a more detailed description of the *Spitzer* data, including reduction techniques, we refer the reader to Smith et al. (2007b).

Spitzer-IRS spectra were extracted using CUBISM (Smith et al. 2007a). Broad spectral features and the mid-IR lines were fit and decomposed using PAHFIT (Smith et al. 2007b). We fix the silicate absorption optical depth at zero, as Smith et al. (2007b) found that negligible amounts of absorption from silicate dust were needed to reproduce the equivalent widths of lines in kiloparsec scale regions of IRS spectral observations of NGC 628. We only accept data with a surface brightness larger than three times the root mean square noise as physically meaningful detections. The hydrogen (7–4) transition at 12.36 μm was not seen in the *Spitzer*-IRS data, leading us to rely on optical lines to determine the H^+ ions.

2.4. H II Region Sample

We use 20″ apertures, which, at the distance of NGC 628, $\sim$9 Mpc (Herrmann et al. 2008; Felipe et al. 2010), correspond to an aperture approximately 900 pc in diameter; these apertures are shown in Figure 2. This size of aperture will likely encompass several individual H II regions that are all located within the same region of a given spiral arm. We select this large aperture due to (1) the beam size of *Herschel*, $\sim$8″; (2) the incomplete filling factor of the PINGS spectral map; and (3) the ability to ensure the inclusion of extended emission associated with each

Table 2
Line Fluxes Relative to Hβ

	Region 1 +50.6, +46.9	Region 2 −55.5, +84.0	Region 3 −37.6, +112.7	Region 4 +41.7, −122.1	Region 5 −59.2, −112.4	Region 6 −40.2, −158.9	Region 7 +80.4, −138.8
[O III] 88 μm	0.85 ± 0.07	1.33 ± 0.01	1.36 ± 0.03	1.79 ± 0.01	1.63 ± 0.21	2.97 ± 0.01	1.62 ± 0.13
[O III] 4959 Å	0.13 ± 0.02	0.12 ± 0.02	0.11 ± 0.02	0.18 ± 0.03	0.27 ± 0.04	0.47 ± 0.08	0.13 ± 0.02
[O III] 5007 Å	0.36 ± 0.05	0.39 ± 0.06	0.45 ± 0.06	0.54 ± 0.08	0.78 ± 0.11	1.44 ± 0.20	0.30 ± 0.04
[O II] 3727 Å	2.33 ± 0.22	2.17 ± 0.16	1.35 ± 0.16	1.80 ± 0.23	2.23 ± 0.17	2.06 ± 0.17	1.80 ± 0.16
[N II] 6548 Å	0.28 ± 0.03	0.27 ± 0.03	0.37 ± 0.04	0.26 ± 0.03	0.20 ± 0.03	0.18 ± 0.03	0.34 ± 0.03
[N II] 6584 Å	0.81 ± 0.08	0.79 ± 0.08	1.06 ± 0.11	0.76 ± 0.08	0.58 ± 0.08	0.51 ± 0.08	0.97 ± 0.08
[S II] 6717 Å	0.48 ± 0.05	0.48 ± 0.05	0.30 ± 0.03	0.41 ± 0.05	0.35 ± 0.05	0.31 ± 0.05	0.47 ± 0.05
[S II] 6731 Å	0.33 ± 0.03	0.32 ± 0.03	0.22 ± 0.02	0.28 ± 0.03	0.26 ± 0.03	0.22 ± 0.03	0.35 ± 0.03
Hα/Hβ	3.86 ± 0.20	4.24 ± 0.14	4.71 ± 0.14	3.70 ± 0.21	3.79 ± 0.15	3.49 ± 0.15	3.39 ± 0.14

Note. Coordinates for regions are given as offsets in seconds of arc from the center of NGC 628, $01^h36^m41\overset{s}{.}7$ $+15^d47^m01^s$.

Table 3
Derived Quantities for H II Regions

	Region 1	Region 2	Region 3	Region 4	Region 5	Region 6	Region 7
R/R_{25}[a]	0.32	0.38	0.22	0.41	0.48	0.52	0.41
[S III]18/33	...	...	0.65 ± 0.03	0.75 ± 0.04	0.92 ± 0.03	0.55 ± 0.03	0.65 ± 0.03
[Ne III]/[Ne II]15/12	...	...	0.14 ± 0.01	0.24 ± 0.01	0.18 ± 0.01	1.09 ± 0.05	0.19 ± 0.01
T_e([O III]) [K][b]	$5950 \pm {}^{450}_{600}$	$5500 \pm {}^{450}_{650}$	$5610 \pm {}^{450}_{450}$	$5550 \pm {}^{500}_{700}$	$6050 \pm {}^{500}_{600}$	$6100 \pm {}^{350}_{350}$	$5050 \pm {}^{700}_{5050}$
O^{++}/O^+	0.50 ± 0.03	0.67 ± 0.03	1.24 ± 0.03	1.15 ± 0.03	1.10 ± 0.03	2.16 ± 0.03	0.76 ± 0.03
12+log(O/H)							
PT05[c]	8.30 ± 0.20	8.33 ± 0.20	8.55 ± 0.22	8.47 ± 0.23	8.41 ± 0.19	8.48 ± 0.18	8.40 ± 0.21
KK04[d]	9.03 ± 0.20	9.04 ± 0.20	9.09 ± 0.22	9.05 ± 0.23	9.00 ± 0.19	8.94 ± 0.18	9.07 ± 0.21
PG12[e]	8.61 ± 0.20	8.65 ± 0.20	8.88 ± 0.22	8.79 ± 0.23	8.73 ± 0.19	8.80 ± 0.18	8.71 ± 0.21
Mid-IR	...	...	8.84 ± 0.18	8.76 ± 0.18	8.80 ± 0.18	8.69 ± 0.18	8.92 ± 0.18
Far-IR[f]	8.45 ± 0.11	8.56 ± 0.10	8.47 ± 0.09	8.59 ± 0.09	8.56 ± 0.13	8.71 ± 0.09	8.63 ± 0.11

Notes.
[a] Inclination corrected, $R_{25} = 315'' = 13.7$ kpc.
[b] Temperature assuming the [S II] low density limit of 100 cm^{-3}.
[c] Pilyugin & Thuan (2005).
[d] Kobulnicky & Kewley (2004).
[e] Peña-Guerrero et al. (2012).
[f] An additional 0.12 dex must be added to account for depletion onto dust grains when comparing with PG12, stellar abundances, and models of chemical evolution.

H II region. Line ratios for each region are reported in Table 2 and derived quantities are reported in Table 3.

3. RESULTS

We will show that the 88 μm/Hβ line ratio alone can provide a much tighter constraint on the O^{++} abundance than the optical line ratio (5007 Å/Hβ), particularly in a high-metallicity environment where temperature sensitive lines are difficult to detect. With additional constraints on density, from [SII] 6716/6731 Å and [SIII] 18/33 μm ratios, and on temperature, from optical to far-IR line ratio, we can obtain even a tighter constraint on the abundance.

3.1. Dependencies in Determining Abundances

Far-IR emission from O^{++} has a low excitation temperature of 163 K (Draine 2011). Therefore, if O^{++} exists in a typical nebula, the 88 μm fine-structure line will be present. In Figure 4, we show the range of O^{++} abundances possible given the average emission line ratios observed in NGC 628 from the de-reddened optical and far-IR spectral maps. We use the five level atom, via the FIVEL program (De Robertis et al. 1987), to derive emissivities for the optical (5007 Å), and far-IR (88 μm) [O III] lines and Hβ at 5000 K and 15,000 K, respectively. These temperatures were chosen because they approximate the observed range of electron temperatures in H II regions.

As is evident, the ratio of [O III] 88 μm/Hβ places a stronger restriction on the possible abundance of O^{++} present compared to the ratio of [O III] 5007 Å/Hβ. However, this ratio is also somewhat sensitive to the electron density of the H II region, unlike the ratio of 5007 Å/Hβ at low densities. We use Hβ relative to 88 μm because our data do not contain mid-IR hydrogen lines, such as the Humphreys-α line, which might otherwise be used in a measure of relative abundance. We constrain the density via PINGS observations of the [S II] 6716/6731 Å ratio. Observations of the [S II] doublet in the optical confirm that these regions are in the low-density limit (see Table 3; e.g., $n_e \lesssim 100$ cm^{-3}; Draine 2011). In regions with *Spitzer*-IRS coverage, the [S III] 18/33 μm ratio confirms the low density.

To establish a lower limit on the density, we calculate the emission measure, EM, determined from the Hβ surface brightness, $I_{H\beta}$,

$$\mathrm{EM} = \frac{4\pi \times I_{H\beta}}{h\nu_{H\beta} \times \alpha^{\mathrm{eff}}_{H\beta}} = \int n_{H^+} n_e dl, \quad (1)$$

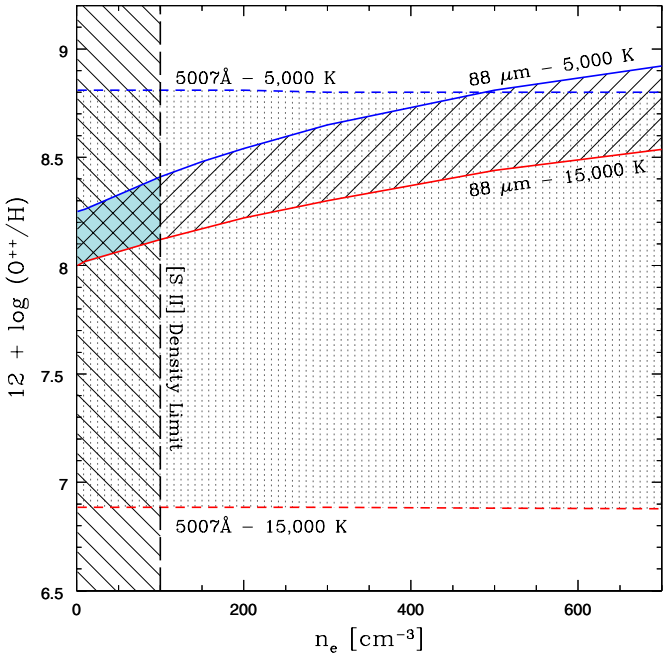

Figure 4. Plausible range of O^{++} abundance (here in units of $12 + \log(O^{++}/H)$) as a function of electron density (n_e) for the average values of 5007 Å/Hβ and 88 μm/Hβ in our selected H II regions in NGC 628. The horizontal dashed lines show the possible range of abundances that can be derived from the ratio of 5007 Å/Hβ. The solid lines bound the possible range of abundances given the 88 μm far-IR emission line. The [S II] low density limit is indicated by the vertical long-dashed line, because all regions are in this limit, the density is constrained to lie to the left of this line. The final range of abundances for this set of line ratios, given no information about the temperature, is highlighted in light blue, at the union of all the other regions. The possible range of $12+\log(O^{++}/H^{+})$ is greatly reduced with the addition of the far-IR fine-structure line.

(A color version of this figure is available in the online journal.)

where $\alpha^{\rm eff}_{\rm H\beta}$ is the effective recombination rate for Hβ, and l is the line-of-sight length through the H II region (e.g., Osterbrock & Ferland 2006). We find that the EM, in our sample of H II regions, lies between 4×10^4–2×10^5. To form a conservative estimate, we assume that each H II region complex fills each 900 pc aperture and has a filling factor of 0.1 (Osterbrock & Flather 1957). This yields lower density limits in the range 20–40 cm^{-3}. These density limits, $30 \leqslant n_e \leqslant 100$, constrain the possible abundance determined from the ratio of [O III] 5007 Å/Hβ.

3.2. Abundances Estimates

3.2.1. Empirical Abundances: KINGFISH + PINGS

Given the depth of the PINGS optical spectra and the relatively high oxygen abundance, we are unable to accurately measure the temperature sensitive [O III] 4363 Å line in any region of NGC 628. We can, however, directly determine the temperature of these regions by comparing the strong lines in the optical and far-IR regimes. We show diagnostic plots, derived from a simple five-level atom, of this temperature determination in Figure 5. While the 88 μm fine-structure line is sensitive to the electron density of the gas (see Figure 4), it can be used in conjunction with the [O III] 5007 Å line, which has a significantly different excitation energy, to constrain the average electron temperature in the O^{++} region of an H II region.

As discussed in Section 2.1, we assume that the aperture correction derived for Hα, to correct the PINGS maps for incomplete sampling of the area subtended by the PINGS field-of-view, could be applied to all emission lines. Given our large aperture and relatively extended H II regions, this is a reasonable assumption. However, such a procedure can also lead to systematic errors and care must be taken. Comparison of the peaks and profiles of the selected regions with the layout of the PMAS fibers indicates that PINGS mapping missed the central emission peak of Region 3, skewing the ratio of [O III]/[O II] emission. Though this aperture exhibits a low far-IR abundance given its proximity to the galaxy center, none of the strong-line abundances show a similar low abundance compared with other similarly calibrated abundances. Due to uncertainties in the world coordinate system of PINGS fibers, we are unable to assign accurate quantitative estimates of the uncertainty due to

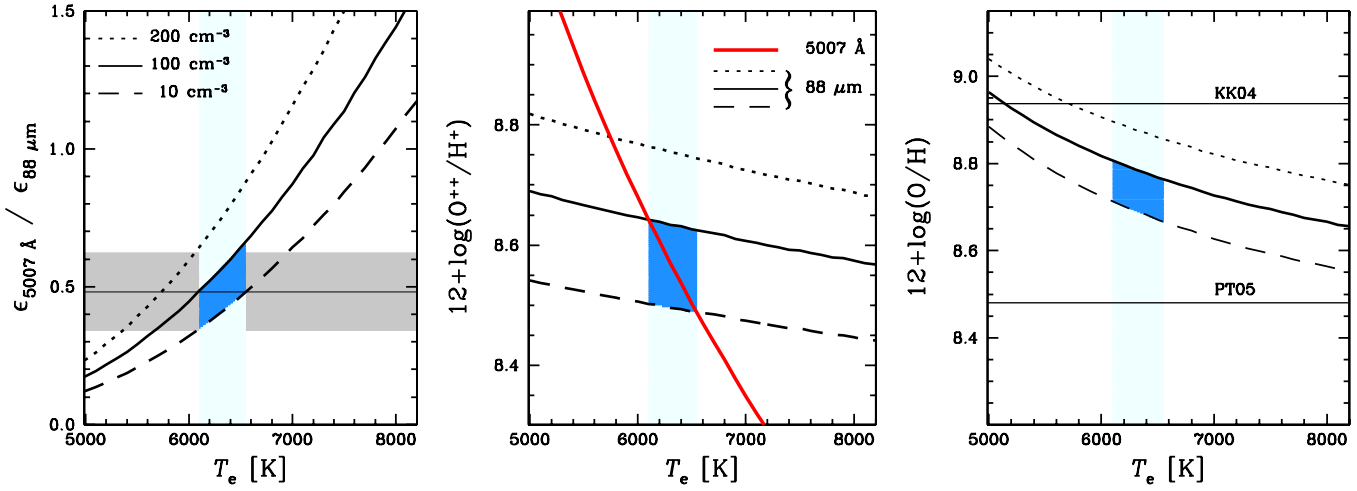

Figure 5. Temperature and abundance constraints on Region 6 (see Figure 2). Left: the ratio of the 5007 Å and 88 μm [O III] emissivities plotted as a function of electron temperature. The different curves show the ratio at different densities; these densities are the same in all panels. The observed flux ratio for this region is indicated by the horizontal line; its uncertainty is shown by the gray shaded area. Center: the abundance of O^{++}, as determined from the 88 μm (black) and 5007 Å (red) lines relative to Hβ, is plotted as a function of temperature. Right: the total oxygen abundance is shown as a function of temperature. For comparison, the abundance determined from the strong optical lines using the KK04 and the PT05 calibrations are indicted by the horizontal lines. In all panels, the vertical blue bar marks the likely temperature inferred from this line ratio. The darker segment of the blue bar highlights the restricted parameter space given that [S II] and [S III] lines indicate the region is in the low density limit.

(An extended, color version of this figure is available in the online journal.)

fiber placement for each region. It is only because of the obvious mismatch of Region 3 that we detected this effect. Though we do not see indications that other apertures were affected, it is certain that all apertures were affected by this systematic error to some extent.

As previously noted, though the optical lines are much more sensitive to temperature changes compared with the far-IR [O III] emission, the far-IR lines are more dependent on the density of the gas, as shown in Figure 4. Given the range of densities that fall in the low density limit, there is a systematic uncertainty of ∼0.05 dex in the abundance determination due to density uncertainties.

One of the largest uncertainties in our far-IR abundance determination is the abundance of O^+, as we do not have a temperature insensitive constraint on this ion. The low temperatures indicated by the ratio of the 5007 Å and 88 μm [O III] lines show that ∼30%–60% of oxygen is singly ionized, depending on the assumed temperature. In order to derive the O^{++}/O^+ ratio, we must find a temperature of the O^+ region. This requires an assumption since we do not have a temperature constraint on this ion. One possible assumption is the two-zone approximation (e.g., Pagel et al. 1992), but this assumption may break down. For example, it is not clear that empirical two-zone approximations (e.g., Pagel et al. 1992; Garnett 1992) are independent of temperature fluctuations; neither is it clear that these relations can be extrapolated to these cool temperatures. Oey & Shields (2000) found that two-zone photoionization models of H II regions in the Large Magellanic Cloud are more consistent with an isothermal nebula when T[O III] < 10,000 K. Additionally, Pilyugin et al. (2010) found that metal-rich SDSS galaxies lie below the empirical calibrations (i.e., lower T[O II] for a given T[O III]). The empirical two-zone relations suggest that T[O II] is greater than T[O III] by approximately 1200 K on average in the H II regions selected in this study. Given the high metallicity and low temperatures, we adopt the average of an isothermal nebula model, where T[O II] = T[O III] (Oey & Shields 2000), and the Garnett (1992) temperature relation,

$$T([\mathrm{O\,II}]) = 0.7 \times (T([\mathrm{O\,III}]) + 0.3). \quad (2)$$

Adoption of either temperature model changes the derived abundances by ∼0.07 dex compared with the far-IR abundances reported in Table 3.

Below we summarize the sources of error we consider, in addition to random errors and errors originating in measuring spectral lines.

1. PPAK scaling to correct for incomplete coverage could produce a random error as large as ∼0.2 dex. In most cases, the agreement with the mid-IR abundances suggests the actual error is typically lower than this; see Section 3.2.2.
2. For our abundances, we assumed n_e lies mid-way between the upper and lower density limits. This could introduce an error of ∼0.05 dex.
3. A two-zone temperature structure following Equation (2) would lower the far-IR abundances by 0.07 dex; adoption of an isothermal temperature structure would raise the far-IR abundances by 0.07 dex.

3.2.2. Abundances from Photoionization Models: KINGFISH + SINGS

The conversion from O^{++}/H^+ to O/H requires some constraint on the abundance of O^+ (or on the ratio of O^+/O^{++}). Although we cannot directly constrain the abundance of O^+ using emission lines from the mid-IR, we are able to use the mid-IR [Ne III]/[Ne II] ratio to constrain the local ionization parameter and metallicity independent of the temperature of the HII region. In Figure 6, we plot the ratio of [O III] 88 μm/Hα against the [Ne III] 15.5 μm/[Ne II] 12.8 μm ratio for the five regions that have *Herschel* PACS, *Spitzer* IRS, and PPAK coverage. We extract the Hα flux from narrow band images that were corrected for [N II] emission. As the mid-IR spectral maps are fully sampled, we use the imaging data to ensure that uncertainties due to the incomplete coverage of the PINGS maps do not influence this measurement of the metallicity.

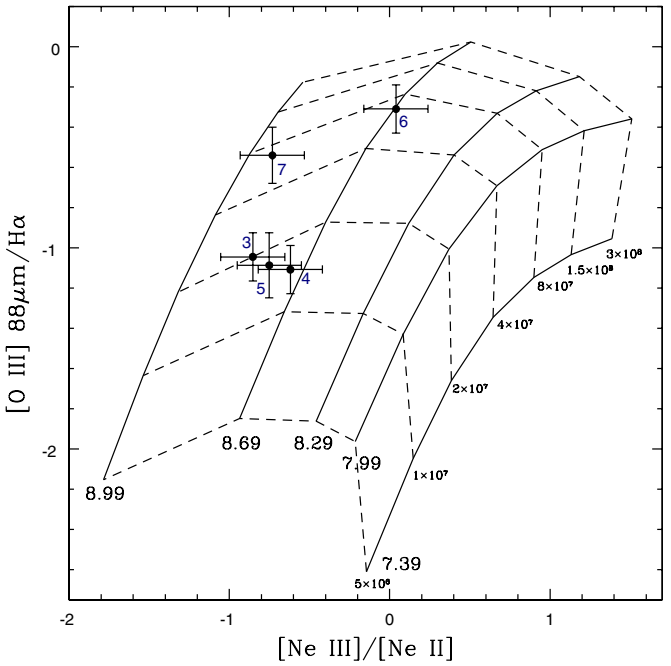

Figure 6. Ratio of [O III] 88 μm/Hα is plotted against the [Ne II] 12.8 μm/[Ne III] 15.5 μm ratio for regions with both PACS and IRS coverage (see Figure 2 for the identification of the regions). We constrain the ionization parameter and metallicity by using the mid-IR Ne ratio in conjunction with [O III] 88 μm, none of which are sensitive to the temperature. A grid of metallicity and ionization parameter from the Mappings III photoionization code is overlaid on the data. Though the metallicity sampled by the models is sparse, we find good agreement with the empirical abundances derived using the PACS and PINGS data.

In Figure 6, we overlay a photoionization model from the Mappings III photoionization code (Groves & Allen 2010), assuming a continuous star formation rate and an average density of 10 cm^{-3}. The assumption of continuous star formation could lead to a systematic underestimate of the metallicity by ∼0.3 dex. We find there is rough agreement between the metallicity indicated by the photoionization model in Figure 6 and the abundance derived by scaling the [O III] temperature (see Table 3 and Figure 7). The largest uncertainty in this case is the lack of a finer grid of metallicity in Mappings III. Though Region 3 shows an anomalously low abundance (see Figure 7), compared with a typical gradient, when combining the KINGFISH and PINGS data, it does not appear to exhibit a discrepant abundance when using the mid-IR Ne lines.

3.3. Comparison to Previous Estimates

Stasińska et al. (2013) used recent mid-IR observations to dispute the presence of temperature fluctuations in H10103, a metal-rich H II region in M101. Though our current data do not allow us to directly investigate the presence of temperature fluctuations in our regions, we can compare our far-IR derived

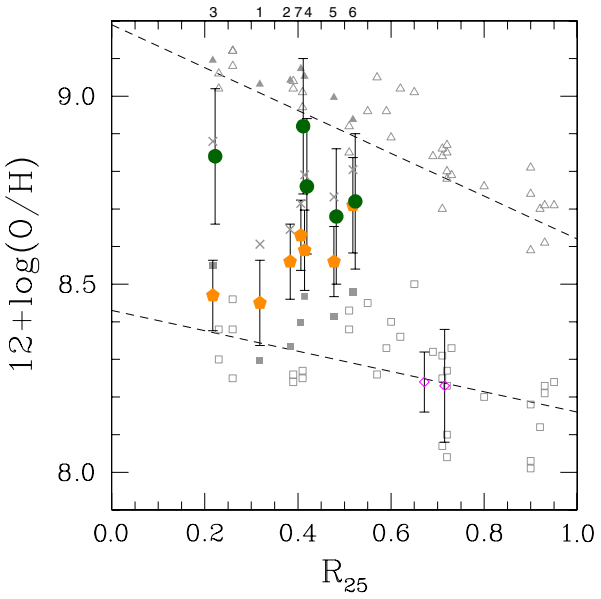

Figure 7. Radial abundance gradient in NGC 628. Gas-phase abundances determined using the KINGFISH and PINGS data are plotted as orange pentagons; abundances determined using KINGFISH and *Spitzer*-IRS data are plotted as filled green circles, slightly offset in radius for plotting clarity. Gray squares, triangles, and crosses represent PT05, KK04, and PG12[2] abundances, respectively. Magenta diamonds indicate direct abundance determinations. Filled points denote the seven regions selected in this study; unfilled points are taken from observations of H II regions reported in Moustakas et al. (2010) and Castellanos et al. (2002). The radial gradient(s) found by Moustakas et al. (2010) are plotted as dashed lines. Regions are identified by their number across the top of the plot.

(A color version of this figure is available in the online journal.)

abundances with the strong-line calibration of Peña-Guerrero et al. (2012, hereafter PG12), which is based on observations of H II regions for which there is a measurement of the temperature inhomogeneity parameter, t^2.

The PG12 calibration includes a correction to account for oxygen that has depleted onto dust grains. This allows their abundances to be directly compared with stellar abundances and models of chemical evolution, which rely on total abundance and not gas-phase abundances (Peimbert & Peimbert 2010). Adopting this correction increases our far-IR abundances by 0.12 dex, bringing the far-IR abundances into better agreement with the mid-IR abundances based on models which include dust. We only include this correction when comparing the abundances with PG12, as this correction has not been adopted for the PT05 or KK04 calibrations.

We find that the average (excluding Region 3) far-IR determined abundance is offset by 0.15, −0.46, and −0.05 dex from PT05, KK04, and PG12, respectively. Thus, though significant offsets exist with both PT05 and KK04, we find that abundances estimated from temperature insensitive far-IR lines are in agreement with the strong line abundances derived from PG12, which have accounted for an average temperature fluctuation.

We plot the inclination corrected gas-phase radial abundance gradient of NGC 628 in Figure 7, assuming an inclination of 6.°5. The far-IR determined abundances, derived from simple five-level atom physics, are plotted as orange pentagons, with PT05, KK04, and PG12[16] strong-line abundances for the same regions plotted as filled gray squares, triangles, and crosses respectively. We also plot the gradient from mid-IR abundances (see Figure 6), based on more complex photoionization models, as green pentagons, for the five regions with *Spitzer*-IRS data. Direct abundances reported by Castellanos et al. (2002) for two H II regions in NGC 628 are also shown as magenta diamonds. Though both regions lie well below our far-IR abundances, they also lie at significantly larger radius, making direct comparison with our sample difficult. This could imply the presence of a relatively steep abundance gradient; it could also imply that temperature fluctuations are important because they would cause these direct abundance determinations to increase. Strong-line abundances from additional H II regions, compiled from the literature by Moustakas et al. (2010), are plotted as open gray triangles (KK04) and squares (PT05). The random errors associated with strong-line abundances are comparatively small, ∼0.05 dex, because the strong-line fluxes are strong. However, such error bars do not display the inherent uncertainty of the calibration.

We do not attempt to fit an abundance gradient to NGC 628, given the restricted range of R_{25} in our data sample. As can be seen in Figure 7, the strong-line abundances for the seven far-IR selected regions resides in-between the PT05 and KK04 gradients derived by Moustakas et al. (2010), which are plotted as dashed lines.

4. CONCLUSIONS

By combining spatially resolved spectroscopy from *Herschel* PACS, *Spitzer* IRS, and PMAS, we derive the gas-phase oxygen abundance of several H II regions in NGC 628 using both optical and far-IR fine-structure lines. The ratio of far-IR fine-structure lines to the hydrogen recombination lines has the advantage of being nearly temperature insensitive. This indifference of metallicity-sensitive ratios to the electron temperature is paramount to being able to unambiguously calibrate oxygen abundances from nebular emission. Though these lines have been observed previously by *ISO*, *Herschel* has enabled observations on sub-kiloparsec scales in galaxies outside the local group. Further, advances in optical integral field unit spectroscopy make it possible to easily match the larger apertures required by observing in the far-IR.

We derive abundances for seven regions in NGC 628 using the far-IR [O III] 88 μm line in combination with optical spectroscopy. The derived abundances lie between the KK04 and PT05 abundances reported by Moustakas et al. (2010) for the radial position of the H II regions here studied. The far-IR abundances are consistent with the PG12 strong-line calibration, which attempts to account for temperature fluctuations that may exist within H II regions when accounting for depletion of oxygen onto dust grains as was considered in this calibration. Our abundance determination utilizes the optical [O II] emission to quantify the O^+ abundance, which retains a reliance upon the temperature determined. Thus, we derive an O^{++} temperature consistent with the infrared observations using the ratio of [O III] 88 μm/5007 Å, and convert that temperature to an appropriate O^+ temperature.

Using Mappings III models (Groves & Allen 2010), we find a good agreement between the empirical far-IR abundances and model based abundances derived using the ratio of the mid-IR [Ne II] and [Ne III] lines and the ratio of [O III] 88 μm/Hα, both of which are insensitive to temperature. These data do not span a large range of radius. They are consistent with the absence of a gradient and with slope of the gradient derived by Moustakas

[16] This calibration includes a correction for depletion of oxygen onto dust.

et al. (2010), assuming different intercepts. Accordingly, we do not attempt to derive an abundance gradient for NGC 628.

NGC 628 is only one of the KINGFISH galaxies for which detections of [O III] 88 μm have been obtained. Out of 54 galaxies in the KINGFISH sample, 40 have detections of [O III] 88 μm, permitting similar studies spanning a wide parameter space. We are expanding the sample of galaxies with the requisite observations that will provide matched optical spectra to selected star-forming galaxies from KINGFISH. From a statistically significant sample of H II regions, we will be able to provide a re-calibration of the strong-line abundance scales that is based on the far-IR [O III]. This scale will be significantly less sensitive to the temperature of an H II region, extending empirical calibrations to the high abundances and low temperatures that have been as yet inaccessible.

We thank the referee for a quick and thoughtful report that has improved this paper. K.V.C. thanks Rick Pogge and Brett Andrews for enlightening discussions on this topic. PACS has been developed by a consortium of institutes led by MPE (Germany) and including UVIE (Austria); KU Leuven, CSL, IMEC (Belgium); CEA, LAM (France); MPIA (Germany); INAF-IFSI/OAA/OAP/OAT, LENS, SISSA (Italy); IAC (Spain). This development has been supported by the funding agencies BMVIT (Austria), ESA-PRODEX (Belgium), CEA/CNES (France), DLR (Germany), ASI/INAF (Italy), and CICYT/MCYT (Spain). HIPE is a joint development by the Herschel Science Ground Segment Consortium, consisting of ESA, the NASA Herschel Science Center, and the HIFI, PACS and SPIRE consortia. This work is based (in part) on observations made with *Herschel*, a European Space Agency Cornerstone Mission with significant participation by NASA. Support for this work was provided by NASA through an award issued by JPL/Caltech. This research has made use of the NASA/IPAC Extragalactic Database (NED), which is operated by the Jet Propulsion Laboratory, California Institute of Technology, under contract with the National Aeronautics and Space Administration.

REFERENCES

Aniano, G., Draine, B. T., Gordon, K. D., & Sandstrom, K. 2011, PASP, 123, 1218
Asplund, M., Grevesse, N., Sauval, A. J., & Scott, P. 2009, ARA&A, 47, 481
Brauher, J. R., Dale, D. A., & Helou, G. 2008, ApJS, 178, 280
Castellanos, M., Díaz, A., I., & Terlevich, E. 2002, MNRAS, 329, 315
Dale, D. A., Aniano, G., Engelbracht, C. W., et al. 2012, ApJ, 745, 95
De Robertis, M. M., Dufour, R. J., & Hunt, R. W. 1987, JRASC, 81, 195
Dinerstein, H. L. 1990, in The Interstellar Medium in Galaxies, ed. H. A. Thronson, Jr. & J. M. Shull (Dordrecht: Kluwer), 257
Dopita, M. A., Kewley, L. J., Heisler, C. A., & Sutherland, R. S. 2000, ApJ, 542, 224
Draine, B. T. 2011, Physics of the Interstellar and Intergalactic Medium (Princeton, NJ: Princeton Univ. Press)
Esteban, C., Bresolin, F., Peimbert, M., et al. 2009, ApJ, 700, 654
Felipe, O. E., Hamuy, M., Pignata, G., et al. 2010, ApJ, 715, 833
García-Rojas, J., & Esteban, C. 2007, ApJ, 670, 457
Garnett, D. R. 1992, AJ, 103, 1330
Garnett, D. R., Edmunds, M. G., Henry, R. B. C., & Skillman, E. 2004, AJ, 128, 2772
Groves, B. A., & Allen, M. G. 2010, NewA, 15, 614
Herrmann, K. A., Ciardullo, R., Feldmeier, J. J., & Vinciguerra, M. 2008, ApJ, 683, 630
Houck, J. R., Roellig, T. L., van Cleve, J., et al. 2004, ApJS, 154, 18
Hummer, D. G., & Storey, P. J. 1987, MNRAS, 224, 801
Kennicutt, R. C., Jr., Armus, L., Bendo, G., et al. 2003, PASP, 115, 928
Kennicutt, R. C., Jr., Calzetti, D., Aniano, G., et al. 2011, PASP, 123, 1347
Kennicutt, R. C., Jr., Hao, C.-N., Calzetti, D., et al. 2009, ApJ, 703, 1672
Kessler, M. F., Steinz, J. A., Anderegg, M. E., et al. 1996, A&A, 315, L27
Kewley, L. J., & Ellison, S. L. 2008, ApJ, 681, 1183
Kobulnicky, H. A., & Kewley, L. J. 2004, ApJ, 617, 240 (KK04)
Martín-Hernández, N. L., Peeters, E., Morisset, C., et al. 2002, A&A, 381, 606
Morisset, C., & Georgiev, L. 2009, A&A, 507, 1517
Moustakas, J., Kennicutt, R. C., Jr., Tremonti, C. A., et al. 2010, ApJS, 190, 233
Muñoz-Mateos, J. C., Gil de Paz, A., Zamorano, J., et al. 2009, ApJ, 703, 1569
Nicholls, D. C., Dopita, M. A., & Sutherland, R. S. 2012, ApJ, 752, 148
O'Donnell, J. E. 1994, ApJ, 422, 158
Oey, M. S., & Shields, J. C. 2000, ApJ, 539, 687
Osterbrock, D., & Flather, E. 1957, ApJ, 129, 26
Osterbrock, D. E., & Ferland, G. J. 2006, Astrophysics of Gaseous Nebulae and Active Galactic Nuclei (3rd ed.; Sausalito, CA: Univ. Science Books)
Ott, S. 2010, in ASP Conf. Ser., Astronomical Data Analysis Software and Systems XIX, ed. Y. Mizumoto, K.-I. Morita, & M. Ohishi (San Francisco, CA: ASP), 139
Pagel, B. E. J., Simonson, E. A., Terlevich, R. J., & Edmunds, M. G. 1992, MNRAS, 255, 325
Peimbert, A., & Peimbert, M. 2010, ApJ, 724, 791
Peimbert, M. 1967, ApJ, 150, 825
Peña-Guerrero, M. A., Peimbert, A., & Peimbert, M. 2012, ApJL, 756, L14 (PG12)
Pilyugin, L. S., & Thuan, T. X. 2005, ApJ, 631, 231 (PT05)
Pilyugin, L. S., Vílchez, J. M., Cedrés, B., & Thuan, T. X. 2010, MNRAS, 403, 896
Poglitsch, A., Waelkens, C., Geis, N., et al. 2010, A&A, 518, L2
Rosales-Ortega, F. F., Kennicutt, R. C., Sánchez, S. F., et al. 2010, MNRAS, 405, 735
Roth, M. M., Kelz, A., Fechner, T., et al. 2005, PASP, 117, 620
Sánchez, S. F., Rosales-Ortega, F. F., Kennicutt, R. C., et al. 2011, MNRAS, 410, 313
Simpson, J. P., Rubin, R. H., Colgan, S. W. J., Erickson, E. F., & Haas, M. R. 2004, ApJ, 611, 338
Smith, J. D. T., Armus, L., Dale, D. A., et al. 2007a, PASP, 119, 1133
Smith, J. D. T., Draine, B. T., Dale, D. A., et al. 2007b, ApJ, 656, 770
Stasińska, G. 2002, RMxAC, 12, 62
Stasińska, G. 2005, A&A, 434, 507
Stasińska, G., Morisset, C., Simón-Díaz, S., et al. 2013, A&A, 551, 82
Stasińska, G., & Szczerba, R. 2001, A&A, 379, 1024